Hong Nhan Nong, Hoang Phi Tran, Camillo Spöri, Malte Klingenhof, Lorenz Frevel, Travis E. Jones, Thorsten Cottre, Bernhard Kaiser, Wolfram Jaegermann, Robert Schlögl, Detre Teschner* and Peter Strasser*

The Role of Surface Hydroxylation, Lattice Vacancies and Bond Covalency in the Electrochemical Oxidation of Water (OER) on Ni-Depleted Iridium Oxide Catalysts

https://doi.org/10.1515/zpch-2019-1460
Received May 2, 2019; accepted July 7, 2019

Abstract: The usage of iridium as an oxygen-evolution-reaction (OER) electrocatalyst requires very high atom efficiencies paired with high activity and stability. Our efforts during the past 6 years in the Priority Program 1613 funded by the Deutsche

***Corresponding authors: Detre Teschner,** Department of Heterogeneous Reactions, Max-Planck-Institute for Chemical Energy Conversion, 45470 Mülheim an der Ruhr, Germany; and Department of Inorganic Chemistry, Fritz-Haber-Institute of the Max-Planck-Society, Faradayweg 4–6, 14195 Berlin, Germany, e-mail: teschner@fhi-berlin.mpg.de; and **Peter Strasser,** Department of Chemistry, Chemical and Materials Engineering Division, Technical University Berlin, Straße des 17. Juni 124, 10623 Berlin, Germany, e-mail: pstrasser@tu-berlin.de
Hong Nhan Nong: Department of Chemistry, Chemical and Materials Engineering Division, Technical University Berlin, Straße des 17. Juni 124, 10623 Berlin, Germany; and Department of Heterogeneous Reactions, Max-Planck-Institute for Chemical Energy Conversion, 45470 Mülheim an der Ruhr, Germany
Hoang Phi Tran, Camillo Spöri and Malte Klingenhof: Department of Chemistry, Chemical and Materials Engineering Division, Technical University Berlin, Straße des 17. Juni 124, 10623 Berlin, Germany
Lorenz Frevel and Travis E. Jones: Department of Inorganic Chemistry, Fritz-Haber-Institute of the Max-Planck-Society, Faradayweg 4–6, 14195 Berlin, Germany
Thorsten Cottre, Bernhard Kaiser and Wolfram Jaegermann: Surface Science Division, Department of Materials Science, Technical University Darmstadt, Otto-Berndt-Strasse 3, Darmstadt, 64287, Germany
Robert Schlögl: Department of Heterogeneous Reactions, Max-Planck-Institute for Chemical Energy Conversion, 45470 Mülheim an der Ruhr, Germany; and Department of Inorganic Chemistry, Fritz-Haber-Institute of the Max-Planck-Society, Faradayweg 4–6, 14195 Berlin, Germany

Forschungsgemeinschaft (DFG) were focused to mitigate the molecular origin of kinetic overpotentials of Ir-based OER catalysts and to design new materials to achieve that Ir-based catalysts are more atom and energy efficient, as well as stable. Approaches involved are: (1) use of bimetallic mixed metal oxide materials where Ir is combined with cheaper transition metals as starting materials, (2) use of dealloying concepts of nanometer sized core-shell particle with a thin noble metal oxide shell combined with a hollow or cheap transition metal-rich alloy core, and (3) use of corrosion-resistant high-surface-area oxide support materials. In this mini review, we have highlighted selected advances in our understanding of Ir–Ni bimetallic oxide electrocatalysts for the OER in acidic environments.

Keywords: iridium; IrNi(Ox); multi-junction photoelectrochemical cell; oxygen-evolution-reaction.

1 Introduction

Solar light is a virtually inexhaustible, hence, renewable energy source. Harvesting and storing its radiation power efficiently and densely, however, continues to be one of today's techno-scientific Grand Challenges [1, 2]. High energy chemical bonds of molecular energy vectors consisting of elements in low redox states formed using free electrons is considered one the most attractive strategies for scalable, future energy storage. The most popular of such energy carriers is hydrogen. Hydrogen can be produced on varying scales by water electrolysis and converted back into electricity using fuel cells. Hydrogen can be used for stationary as well as mobile applications; it can be safely stored and transported over large distances [3]. This is why electrolytic hydrogen has been the center of a vision of a future hydrogen economy [4].

Solar hydrogen (and oxygen) can be produced from the combination of photovoltaic devices with "dark" water electrolyzers, or else using integrated photoelectrochemical cell (PEC) devices incorporating semiconductors and water splitting electrocatalysts, where the semiconductor may or may not be in direct contact with the liquid electrolyte (classic "non-buried" semiconductor-electrolyte junctions vs. buried multi-junction devices with protecting oxide/catalyst top layers) [5–9].

Low-temperature dark water electrolysis can be carried out using (i) liquid alkaline water electrolyzers (AWE), (ii) proton exchange membrane electrolyzers (PEM) and (iii) alkaline exchange membrane electrolyzers (AEM), which however are still at a somewhat lower technology readiness level [10, 11]. Although allowing the use of low-cost non-noble electrodes [12, 13], alkaline electrolysis suffers

from lower electrolyte conductivities and lower load flexibilities (less capable to be operated at varying low partial current loads) [4, 14]. On the other hand, the PEM acidic electrolysis requires noble metal catalysts for both electrodes, the loading of which must be kept at a minimum [15, 16]. The PEC device schemes, on the other hand, require the deployment of at least one, either the hydrogen evolution reaction (HER) or the oxygen evolution reaction (OER) electrocatalyst, or in some configurations also of both electrocatalysts in a layered format on top of conducting oxidic interlayers (buried junctions) or on the semiconductor directly (classical junctions) [17]. While the catalyst materials employed are typically similar Pt and Ir formulations as used in dark electrolyzers, the PEC-based water splitting catalysts operate under distinct boundary conditions and at quite different current densities. In simple terms, catalysts in dark electrolyzers must operate very energy and voltage efficient, while the catalyst in PECs must be particularly inexpensive or deployed in particularly low mass loadings.

While Pt is a nearly ideal catalyst for the HER, on the anodic electrode, the OER is the kinetic bottleneck of water electrolysis due to its sluggish elementary catalytic reaction steps resulting in relative high over-potential [4]. In the 1950s, John Bockris' group explored the OER kinetics and established early mechanistic hypotheses on the critical role of reactive oxygenated surface intermediates, such as hydroxyl (OH), atomic oxygen (O), and peroxide (OOH), using reactive schemes which have kept their principle validity until today [18]. Later, Trasatti established volcano relations between the enthalpy of reaction of the transition of different binary metal oxides from a lower to a higher metal oxidation state and the corresponding experimental OER over-potentials. He found the oxides of Ru and Ir near the top [19, 20]. Much later, density functional theory (DFT) calculations of the anodic electrocatalytic OER provided deeper insight into the origin of the kinetic overpotentials. Computational work using a stepwise OER mechanism, virtually following the scheme set up by Bockris decades earlier, now showed that the oxide surface, where adsorbed oxygen (O_{ad}) is destabilized relative to adsorbed peroxide intermediate (OOH_{ad}), is the expected catalyst [21]. The relatively high kinetic activities of IrO_2 and RuO_2 are attributed to their near optimal binding energy of O_{ad} and OOH_{ad} and their good conductivity [16, 22–24]. Based on the overpotential of OER at a geometric current density of 5 mA cm^{-2}, the general activity trend established for oxidized forms of noble metals was: $Ru > Ir > Rh > Pt > Au$, and the stability was found in the following trend: $Pt > Rh > Ir > Au \geq Ru$ [25–27]. Thereby, Ir has always shown the best trade-off between catalytic activity and stability in acidic electrolyzers, but its extreme low abundance requires atom-efficient low-content chemical architectures to keep the noble metal loading at a scalable level, while maintaining sufficient activity and stability.

Experimental efforts of OER oxide catalyst research undertaken as part of the Priority Program 1613 funded by the Deutsche Forschungsgemeinschaft (DFG) over the past 6 years were geared to study, understand and mitigate the molecular origin of kinetic overpotentials of Ir-based OER catalysts for acidic water oxidation. New materials designs were explored to make Ir-based catalysts more atom efficient, energy efficient, and stable. Approaches addressed involved (1) use of low-Ir content bimetallic mixed metal oxide materials, (2) use dealloying concepts of nanometer-sized core-shell particle with a thin Iridium oxide shell

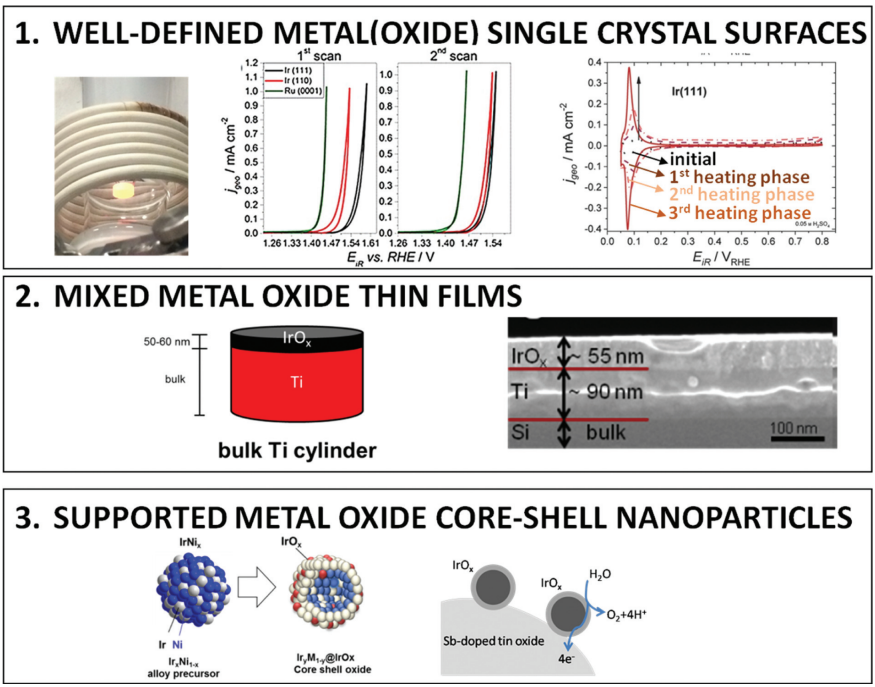

Fig. 1: During the DFG Priority Program 1613 on Photoelectrocatalytic generation of hydrogen, new Ir based metal oxide electrocatalysts for the OER were studied in three levels. One Metallic Iridium Single Crystal level (shown, from left to right, is a Ir(111) crystal during induction-based annealing to 2000 °C, linear scan voltammetry into the OER potential range of Ir(111), Ir(110) and Ru(0001) single crystals, and cyclic voltammograms before and after thermal annealing of the Ir crystals). Two Polycrystalline thin film level (shown is a scheme of the spin-coated Ir oxide thin films on top of a Ti cylinder for Rotating Disk Electrode Measurements, and a cross sectional Scanning electron microscopy (SEM) across a IrO_x film on Ti/Si wafer). Three Nanometer sized core-shell particles supported on high-surface-area oxide supports [shown is the IrNi dealloying scheme to achieve IrO_x core-shell alloy particles, and nanoparticles with IrOx surface supported on Sb-doped tin-oxide (ATO) with a schematic reaction of the OER]. In this mini review, we focus on the latter two.

with a hollow or non-precious-metal-rich particle core, and (3) use of corrosion-resistant high-surface-area oxide support materials. Research work was carried out using three distinct catalyst material concepts, single crystals, polycrystalline thin films, and nanostructured particle ensembles, as shown schematically in Figure 1. Here, we will focus on the latter two.

In this mini review, we highlight some important advances and new insights derived from our work on Ir–Ni bimetallic OER catalysts for use in acid PEM electrolyzers or in PECs. We show how the chemical state and the chemical surface termination of IrNi mixed oxide thin films affect their OER reactivity and stability. Using highly active, metal alloy-derived IrNi@IrO_x core-shell nanoparticles, we also review recent combined experimental and computational insights into the dynamic of the chemical state and local geometric structure of reactive oxygen ligands in hole-doped defective IrO_x lattices probed under operando OER conditions. Our choice of Ni as the second alloying component was motivated by prior work on Pt alloy core shell nanoparticles used for the oxygen reduction reaction at fuel cell cathodes [28–32]. Our idea was to leverage the same surface dealloying mechanism to generate an Ir rich shell on a non-precious-metal-rich core. Aware that the particle surface would invariably transform into an oxide layer under anodic OER conditions, we extended the Ni dealloying potentials far into the anodic range in order to couple the Ni dissolution and Ir oxide formation at the surface of the nanoparticles. Overall, this mini review reflects progress achieved under this DFG funded collaborative project.

2 Results and discussion

As laid out in the Introduction, we divided the Results and Discussion into three sections. In the first, we discuss $IrNiO_x$ thin films for OER that are formed by thermal treatments, whereas in the second we focus our attention to IrNi alloy nanoparticles (NPs) that are electrochemically oxidized. In the final third section, we briefly describe photoelectrochemical tests performed with an $IrNiO_x$ film.

2.1 $IrNiO_x$ oxide thin films

In order to understand the role of Ni-doping on the OER activity of IrO_x electrocatalysts, we have prepared five Ir–Ni mixed oxide thin film catalysts ranging from 21 atomic% (at%) Ni to 89 at% Ni in composition plus additional two reference materials with 0 and 100% Ni, by spin coating and calcination. Coating solutions with 80 g L^{-1} Ir(III) acetate or 105 g L^{-1} Ni(II) acetate tetrahydrate in ethanol were mixed to attain the target Ir:Ni ratios. The solutions were applied onto the

spinning substrate at 200 revolutions per minute (rpm) ensuring full coverage. Thereafter, the rotation velocity was increased to 2000 rpm and dwelled at this velocity for 45 s to finish the spin coating process. The coated samples were calcined in a pre-heated muffle furnace at 450 °C for 15 min. For detailed description of sample preparation and characterization, see [33]. The Ir–Ni mixed oxide catalysts will be referred to as x%Ni–MO (MO for Ir–Ni mixed oxide). Thereby, x specifies the fraction of Ir atoms substituted by Ni (in at%) in the as-prepared mixed oxide. The abbreviation "ap" or "OER" refers to the state of the film "as-prepared" or after "OER", respectively.

Figure 2a depicts quasi-stationary OER polarization curves of the electrocatalysts in 0.1 M $HClO_4$. Clearly, doping Ir with Ni as a mixed oxide provides a beneficial effect on the electrocatalytic OER activity. Catalytic OER current densities at a fixed overpotential of 300 mV (1.530 V_{RHE}) are plotted and compared in Figure 2b as a measure for the OER performance. The geometric and the Ir mass based current density exhibit a volcano type curve with a maximum at high Ni contents (67 at% – 79 at%). Compared to the Ir oxide reference catalyst the OER

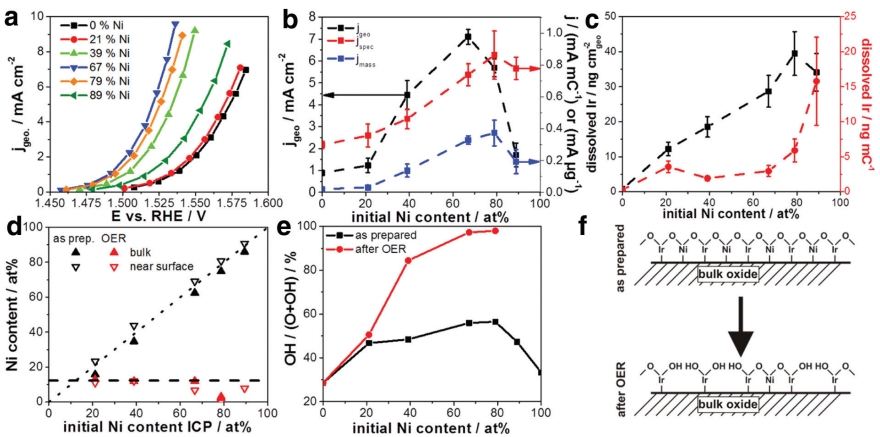

Fig. 2: (a) Quasi-stationary OER polarization curves (iR corrected). (b) Current densities at an OER overpotential of 300 mV (1.530 V vs. RHE) normalized to the electrodes geometric surface area (j_{geo}), the anodic charge q* (j_{spec}) and the applied Ir mass (j_{mass}). (c) Amount of dissolved Ir during 30 min of OER with 1 mA cm^{-2}. The amount of dissolved Ir is provided normalized to the geometric surface area and to q*. (d) Near surface and bulk composition of Ir–Ni mixed oxide films before (MO-ap) and after (MO-OER) the electrocatalytic OER protocol. The Ni content measured by ICP-OES is provided on the x-axis. The near surface Ni content and the bulk Ni content, shown on the y-axis, were determined by X-ray photoelectron spectroscopy (XPS) or, respectively, by averaging XPS depth profiles. (e) Hydroxyl group (OH) fraction to the total oxide related oxygen (hydroxyl groups and both lattice oxygen species) as determined by XPS. (f) Model of Ni leaching from the surface of Ir–Ni mixed oxides. Adapted with permission [33].

performance increased by a factor of ∼8, based on the geometric current density (j_{geo}), or even more remarkably, by a factor of ∼20, based on the Ir mass-based current density (j_{mass}). The surface specific catalytic current density (current normalized by the anodic charge obtained in a fixed window of 0.4–1.4 V RHE) again increased with the Ni content up to 67% Ni–MO (see Figure 2c), but leveled off at higher Ni contents within the accuracy of the measurement. Compared to pure Ir oxide, the surface specific OER activity of samples with an initial Ni content at and above 67% was increased by a factor of about 2.6.

Besides the electrocatalytic activity, the stability is another major concern of OER catalysts. Here the stability against Ir dissolution was measured using potential-resolved online ICP-MS analysis [34, 35] on samples, which previously underwent the electrocatalytic OER protocol. In Figure 2c, the total mass of dissolved Ir during 30 min galvanostatic water electrolysis at 1 mA cm^{-2} is shown as function of the initial Ni content. For our stability discussion, the dissolved Ir mass was normalized to the geometric (black) as well as the surface-charge-normalized catalyst area. Looking at the geometric stability, the amount of dissolved Ir first increased with increasing Ni content and peaked at 79% Ni–MO. At this maximum, the Ir dissolution rate is approximately 47 times higher than that of pure Ir oxide, while in the case of 67%-MO it is 34 times higher. Although this is a substantial drop in Ir stability relative to the pure Ir oxide, we note that even the least stable thermally prepared film catalysts of this study exhibited an Ir dissolution rate that was comparable to electrochemically oxidized Ir metal, and even much lower than electrochemically oxidized Ru metal [35]. Interestingly, geometric OER performance and geometric Ir dissolution rate peaked at different Ni contents. Furthermore, 21% Ni–MO-OER showed a dissolution rate 14 times higher than pure Ir oxide although the geometric OER activity was rather similar. Both observations indicate that the OER activity and stability are not necessarily (anti)correlated. Also, when the amount of dissolved Ir is normalized to the electrochemically active Ir oxide surface area a broad plateau appears at Ni contents $\leq$67 at% (red in Figure 2c). The data in Figure 2b and c evidence that, although the Ir dissolution rate is rather constant across the plateau, the specific OER activity can be tuned and increases with the Ni content. This provides further evidence for the principle possibility of decoupling OER activity and catalyst's stability.

Recently, the stability number (S-number) was introduced as a metric for stability benchmarking of electrocatalysts [36]. The S-number is defined for OER activity-stability of Ir-based catalysts as the ratio of the amount of evolved oxygen and the amount of dissolved Ir. The higher the ratio, the more stable the catalyst is. We calculated the S-numbers of the IrNi mixed oxides for the measurements at a current density of 1 mA/cm^2 for 30 min, assuming 100% Faraday efficiency.

As the result, all mixed oxides showed the S-numbers in the range of 10^4–10^5, similar to those of hydrous IrO_x and $SrIrO_x$ films [36]. Scanning electron microscopy (SEM) imaging after OER (not shown) indicated that catalysts with $\leq$39 at% initial Ni content remained morphologically stable, while the others showed increasing sponge like porosity increasing with higher Ni content. This observation suggests that Ni was increasingly leached out of the materials.

To understand Ni leaching, bulk and near surface composition of MO-ap and MO-OER catalysts were determined and plotted against the initial Ni content, see Figure 2d. The bulk Ni content was determined by averaging X-ray photoelectron spectroscopy (XPS)-sputter depth profiles (solid triangles) and for MO-ap additionally by ICP-OES. Both approaches are in excellent agreement for MO-ap, validating the method of averaging XPS depth profiles for bulk Ni content determination. After OER catalysis, bulk and surface Ni content (red symbols) evidence strong, yet incomplete Ni dissolution. For initial Ni contents $\leq$67 at%, residual Ni values levelled at around 12 at%, likely stabilized through interaction with Ir. This observation is important, as it demonstrates that about 12 at% Ni can be stabilized in the mixed oxide matrix and may contribute to electronic and geometric effects beneficial for the water splitting catalysis.

Grazing incidence X-ray diffraction suggests that the mixed oxides in the most interesting range of 39–89 at% Ni are X-ray amorphous. Selected area electron diffraction, however, evidenced nano-crystallinity with continuous evolution of the broad diffraction pattern. The pattern changed from rutile type structures at low Ni content toward a brucite-like layered structure at high Ni content.

XPS was used to characterize the chemical state of Ir, Ni and O in MO-ap and MO-OER film catalysts. Here we focus our attention to the O 1s region, more details can be found in [33]. Fits of the O 1s spectra (not shown) revealed up to 4 different oxygen species at about 529.2, 529.9, 531.4 and 533.1 eV. The species at $\sim$533.1 eV can be assigned to adsorbed water, whereas the species at 529.9 eV and 531.4 eV are related to lattice oxygen and hydroxyl groups, respectively [37, 38]. The species at 529.2 eV appeared with mixed oxides. The binding energy of lattice oxygen in the metal oxides is a weak function of the Ni content, the pure NiO being located at 529.6 eV. Figure 2e depicts the fraction of surface hydroxyl species (OH-fraction) to the surface oxide related species (OH and both lattice oxygen species). In MO-ap the OH-fraction was just a weak function of the Ni content. The OH fraction after Ni leaching and OER catalysis, however, increased depending on the initial Ni content. Pure Ir oxide showed almost no change in the OH fraction, while films with higher initial Ni contents revealed a much-increased OH fraction; value close to 100% was reached for 67–79% Ni–MO-OER.

When Ni is leached from MO-ap films, oxygen atoms lose binding partners, and to assure electroneutrality, the Ni-depleted oxygen atoms will take up protons

from the electrolyte and, thus form surface hydroxyl groups, as indicated in Figure 2f. Indeed, upon Ni leaching the surface OH fraction increased significantly up to 67% initial Ni content (Figure 2e). Importantly, the surface-specific OER activity revealed a rather similar trend as the OH fraction. Both increase with increasing Ni content and reach saturation at 67% Ni. Thus, we conclude that the ratio of surface hydroxyls to the total surface oxygen atoms is directly related to the surface specific catalytic OER activity of Ir oxides. This trend becomes intuitive if surface OH groups are assumed to act as reactive surface intermediates and/or undergo deprotonation at anodic potentials under OER and form sites that serve as proton acceptor for the deprotonation step of adsorbed water.

With regard to potential Ni-related oxide lattice geometry and strain effects, we point out that a strong increase in the intrinsic catalytic water splitting activity occurred at essentially constant residual Ni contents of about 12 at% Ni in the active oxide films (for initial Ni contents $\leq$67 at%). We therefore conclude that the residual near-surface Ni content is not a suitable quantitative descriptor for OER activity, and oxide lattice strain effects are likely of limited significance.

2.2 Core-shell $IrNi_x$ nanoparticles for OER

Ni rich Ir–Ni bimetallic NPs were synthesized using a previously reported polyol method [39] involving 1,2-tetradecadiol as reducing agent and oleylamine, oleic acid as capping ligands. The NPs were immobilized on high surface area carbon black Vulcan XC 72R supplied by Carbot. For additional details about the synthesis procedure, see [40]. The $IrNi_x$ NP precursor alloys (PA-$IrNi_x$) were first electrochemically dealloyed to form dealloyed metallic core-shell NPs ("D-$IrNi_x$"). Subsequently, they were selectively surface oxidized to form "SO-IrNi@IrO_x" metal oxide core-shell NPs. SO refers to the stepwise nature of the preparation ("SO-$IrNi_x$"). The stepwise oxidized synthesis is depicted schematically in Figure 3a top. Alternatively, DO-IrNi@IrOx were prepared by directly, that is, coupled dealloying/oxidation ("DO-$IrNi_x$"). Note that in the following the SO-$IrNi_x$ or DO-$IrNi_x$ nomenclatures emphasize the stoichiometry of the parent precursor alloy, while the SO-IrNi@IrO_x and DO-IrNi@IrO_x nomenclature stress the chemical core-shell structure.

Supported Ir–Ni bimetallic precursor alloy nanoparticles were synthesized with three different $IrNi_x$ ratios (x = 2.3, 3.3, 5.7). Supported pure Ir nanoparticles were used as a benchmark catalyst. The XRD profiles of the $IrNi_x$ and pure Ir NP catalysts exhibit a peak pattern consistent with a face-centered cubic crystal symmetry. All diffraction lines of Ni-containing samples are shifted toward higher 2θ, indicating a contraction of the lattice with the increasing amount of smaller Ni atoms. The relationship between the lattice constant derived from the (111) lines

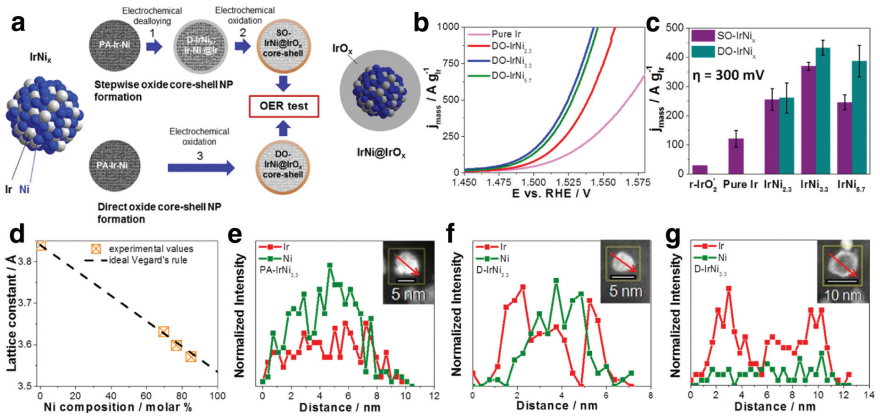

Fig. 3: (a) Synthetic protocol for the preparation of SO-IrNi@IrO$_x$ and DO-IrNi@IrO$_x$ hybrid core-shell nanoparticle catalysts. Precursor IrNi alloys ("PA-IrNi", and alloy scheme on left, blue: Ni, grey: Ir) are stepwise (SO) or directly (DO) dealloyed and surface oxidized. "D-IrNi$_x$" denotes the dealloyed stage. The "SO-IrNi$_x$" or "DO-IrNi$_x$" nomenclatures emphasize the original stoichiometry of the parent precursor alloy, while the "SO-IrNi@IrO$_x$" and "DO-IrNi@IrO$_x$" nomenclature stresses the chemical structure of the core-shell particles. (b) Sweep voltammetry as catalytic OER activities of DO-IrNi$_x$ core-shell nanoparticle catalysts, in comparison to pure Ir nanoparticles. (c) Ir mass based activities at 300 mV overpotential. Conditions: 0.05 M H_2SO_4, 1600 rpm, scan rate 5 mV s^{-1}. "r-IrO$_2$*" denotes the Ir-mass based activity of IrO$_2$ rutile NPs at 300 mV overpotential [41]. (d) The relationship between lattice constant and Ni composition (orange symbols) compared to Vegard's law (dashed line) in the precursor alloys. (e, f, g) STEM-EDX line profiles of Ir and Ni in PA-IrNi$_{3.3}$ (e), and D-IrNi$_{3.3}$ (f and g). The red arrows in the corresponding NPs (see insets) indicate the directions of the EDX line profiles. Adapted with permission [40].

and the composition of the annealed IrNi$_x$ NPs (Figure 3d) followed the Vegard's law reasonably well. In order to confirm our hypothesis about the formation of a metallic core-shell structure, and to get further atomic-scale insight into the nanostructure of the catalysts before and after the dealloying, we performed high-angle annular dark-field imaging (HAADF)-STEM and STEM-EDX line scans of the IrNi$_{3.3}$ material. PA-IrNi$_{3.3}$ catalyst particles possess largely homogeneous chemical composition (Figure 3e). Upon dealloying, the homogeneous Ir, Ni distribution transformed to a core-shell-type line scan of D-IrNi$_{3.3}$ with two symmetric Ir shell peaks (Figure 3f,g). Interestingly, the morphology of the dealloyed nanoparticles strongly depended on particle size. While smaller NPs favored Ni-richer core-shell structures, larger NPs appear to undergo severe Ni leaching in their transition to core-shell structures, with little Ni remaining in the nanoparticles.

To prepare the catalytically active oxidized core-shell structures, dealloyed IrNi@Ir metallic core-shell particles (D-IrNi$_{3.3}$) were electrochemically cycled up

to +1.5 V, where surface Ir atoms are oxidized. For comparison, the homogeneous precursor alloys PA-$IrNi_{3.3}$ were subjected to the same cycling protocol in order to achieve simultaneous Ni dealloying and surface Ir oxidation. Synchrotron-based XPS experiments indicated an essentially complete removal of near-surface Ni upon oxidation. Depth resolved Ir 4f core level spectra confirmed the oxidation of near-surface Ir and the retention of some metallic iridium at larger information depth, indicating an oxidized surface and metallic alloy bulk nanostructure.

SO-IrNi@IrO_x and DO-IrNi@IrO_x core-shell catalysts were subjected to a sweep voltammetry protocol in 0.05 M H_2SO_4. The sweep voltammetry and the Ir-mass-based activities of the samples at 300 mV overpotential are presented in Figure 3b,c. All Ni-containing nanoparticle catalysts are more active for the OER than pure Ir. The most active catalysts are the SO-$IrNi_{3.3}$ and DO-$IrNi_{3.3}$ showing a three times higher mass activity compared to pure Ir. Directly oxidized core-shell catalysts showed even slightly higher OER mass activity than that of stepwise oxidized samples.

Since carbon can undergo oxidative degradation under harsh OER conditions, an attempt was made to prepare high surface area conductive oxide supports. The preparation of mesoporous Sb-, F-, and In-doped SnO_2 powders with high surface area as catalyst supports are described in [42]. Antimony-doped tin oxide showed high surface area, mesoporous structure, good electrical conductivity, and high corrosion resistance, and thus we utilized this material for our IrNi nanoparticles. $IrNi_{3.3}$ nanoparticle precursor alloys supported on mesoporous antimony doped tin oxide ($IrNi_{3.3}$/Meso-ATO) were prepared starting with the synthesis of Meso-ATO powder support using a soft-templating process involving tetradecylamine (TDA) as a template. Thereafter, $IrNi_x$ metallic NPs were synthesized using a polyol method in the presence of 1,2-tetradecandiol as reducing agent and oleic acid, oleylamine as capping agents. Meso-ATO powder was introduced into the reaction mixture before starting the metal reduction. The supported NPs were washed with ethanol, freeze dried and then thermally treated. The preparation of metallic alloy NPs supported on redox active oxides and the removal of capping agents require a careful optimization of a balanced annealing protocol to maintain the chemical state of alloy and support. In order to find an appropriate condition, the materials were annealed at different temperatures (T = 180, 250, 300, 400, 500 °C) in inert N_2 gas, as opposed to our previous procedure in H_2 with the carbon support, to prevent the reduction of the ATO support. The obtained precursor alloys were denoted as PA-$IrNi_{3.3}$/Meso-ATO-T, and later used for synthesis of the core-shell structured catalysts ($IrNiO_x$/Meso-ATO-T). For comparison, pure Ir NPs supported on carbon (Ir/C) were also prepared. The detailed protocols for the synthesis, electrode preparation and characterization of all samples can be found in [43].

The Meso-ATO powder has a mesoporous, foam-like structure consisting of interconnected NPs with high monodispersity. This material provided a surface area as high as 264 $m^2\ g^{-1}$ and thus was much higher than that of commercial ATO (Sigma Aldrich, 47 $m^2\ g^{-1}$). $IrNi_{3.3}$ alloy NPs exhibited a reasonably homogeneous dispersion with a few small agglomerated clusters. The nanoparticle size distribution was in the range of 7.3 ± 2.5 nm. Figure 4a shows an aberration-corrected HAADF-STEM Z-contrast image of the $IrNiO_x$/Meso-ATO-180 catalyst. The dealloyed NPs exhibit dark centers with bright outer shells. Note, under Z-contrast condition the image intensity of Ir (Z = 77) is much higher than that of Ni (Z = 28). The spherical morphologies of the NPs rule out thickness variations as source of the dark particle Z-contrast suggesting a drastically Ir-depleted chemical state of the particle cores surrounded by IrO_x shells. Elemental mapping (Figure 4b) confirmed the core–shell structure. As with the carbon-supported

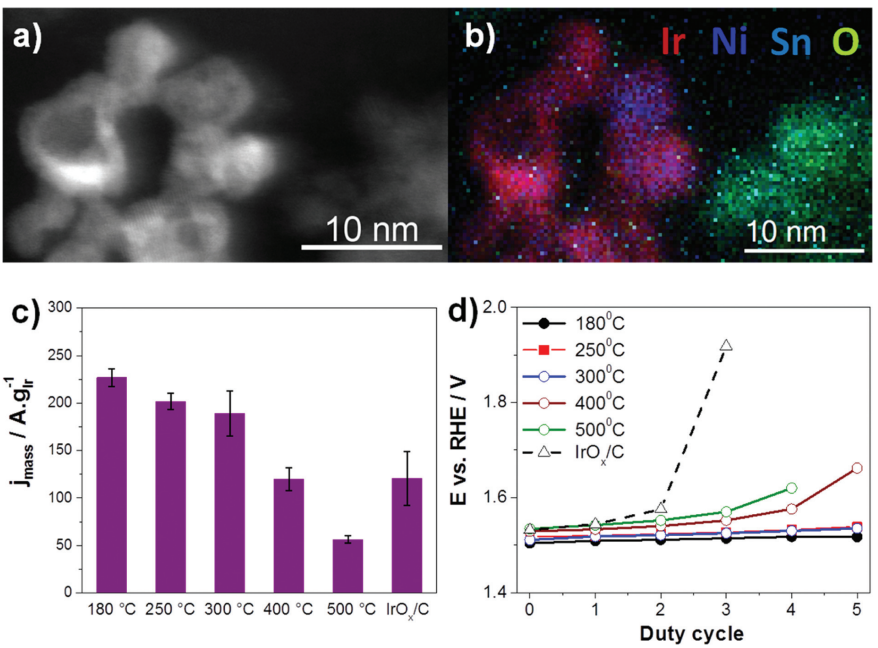

Fig. 4: (a) HAADF-STEM image of the $IrNiO_{3.3}$/Meso-ATO-180 core-shell NP catalyst synthesized from PA-$IrNi_{3.3}$/Meso-ATO-180. (b) Elemental mapping of Figure a (Ir red, Ni blue, Sn dark cyan, O green). (c) Ir-mass-based activity at η = 300 mV overpotential of IrO_x/C and $IrNiO_{3.3}$/Meso-ATO-T. (d) Potential at 1 mA cm^{-2} using linear sweep voltammetry after duty cycles of IrO_x/C and $IrNiO_{3.3}$/Meso-ATO-T. Temperature (T) at which NPs have been treated is given for each data set. Measurement conditions: 0.05 M H_2SO_4, 1600 rpm. The loading of Ir was 10.2 mg cm^{-2}. Adapted with permission [43].

$IrNi_{3.3}$, depth-resolved XPS (not shown) confirmed that upon cycling into OER electrode potentials, the largely metallic precursor alloy gradually depleted in Ni and transformed to a thin IrO_x shell.

The catalysts were subjected to a sweep voltammetry protocol in 0.05 M H_2SO_4, and their Ir-mass-based reactivity at an overpotential of 300 mV are presented in Figure 4c. The $IrNiO_x$/Meso-ATO-T catalysts with $T \leq 300$ °C are significantly more OER active as compared to the IrO_x/C benchmark sample. XPS and HE-XRD PDF results indicated that the precursor alloys annealed at $T \leq 300$ °C maintained the desired IrNi metallic alloy phase. In contrast, the catalysts annealed at 400 °C and 500 °C, showed significantly lower OER activities due to the phase segregation into a NiO and an Ir-rich nanophase. To test the durability of the catalysts under conditions closer to the operating conditions of PEM electrolyzers, we applied a potential-step duty-cycle protocol. In this protocol, the potential was first kept at $E^{0.5}$ (potential at which the current density reached 0.5 mA cm^{-2}) for a period of 10 min, then increased by 20 mV and kept at the new value for 10 min. This increasing step was repeated for five times until the last holding potential E^{final} equaled to $E^{0.5} + 100$ mV. The process was called one duty cycle. The duty cycle was repeated five times, and after each duty cycle, the OER activity was tested. Figure 4d plots the electrode potentials at a current density of 1 mA cm^{-2} measured by linear sweep voltammetry after each duty cycle. The electrode potential of IrO_x/C reached >1.9 V after only two duty cycles, indicating the complete degradation of the catalyst. It is noteworthy to mention the potential passivation of the glassy carbon substrate under high anodic potential and prolonged polarization, which might contribute to the degradation of the catalytic performance [44]. Nevertheless, the duty cycle protocol was set such that the potentials were in the range of 1.5–1.6 V vs. RHE, where the passivation of the glassy carbon was not severe during the course of the measurement [44]. Only in the case of IrO_x/C, after two duty cycles the catalyst performance dropped drastically, requiring higher potentials applied for the 3rd duty cycle and, as the result, contribution of the substrate passivation might be larger. $IrNiO_x$/Meso-ATO annealed at lower T showed higher activity and durability than those samples annealed at 400 and 500 °C. Again, the most active and stable catalyst was the $IrNiO_x$/Meso-ATO-180 material evidencing a successful combination of the activity advantages of core–shell architectures and the durability benefits of an oxide support.

To gain insights into the electronic structure of $IrNiO_x$ core–shell catalysts, we performed X-ray absorption near-edge structure (XANES) measurements using Ir(Ni)O_x (with and without Ni doping) at the iridium L_3 edge [45]. The iridium L_3-edge XANES of iridium compounds are characterized by broad white lines, which primarily correspond to transition from occupied 2*p* to empty 5*d* states [46–48].

Figure 5a shows the white line position of the catalysts at different applied potentials as a function of the formal *d*-band hole count using a slope of 0.925 eV per *d*-band hole obtained from iridium ($5d^76s^2$), $IrCl_3$ ($5d^66s^0$) and IrO_2 ($5d^56s^0$) standards. Note that our derived slope is in excellent agreement with literature values [49, 50, 52]. At +0.4 V_{RHE}, the absolute number of *d*-band holes in IrO_x is between those of the $IrCl_3$ and IrO_2 standards. Based on established iridium electrochemistry [53–56], we expect to see Ir^{iii+} and/or Ir^{iv+} sites at this potential for both the

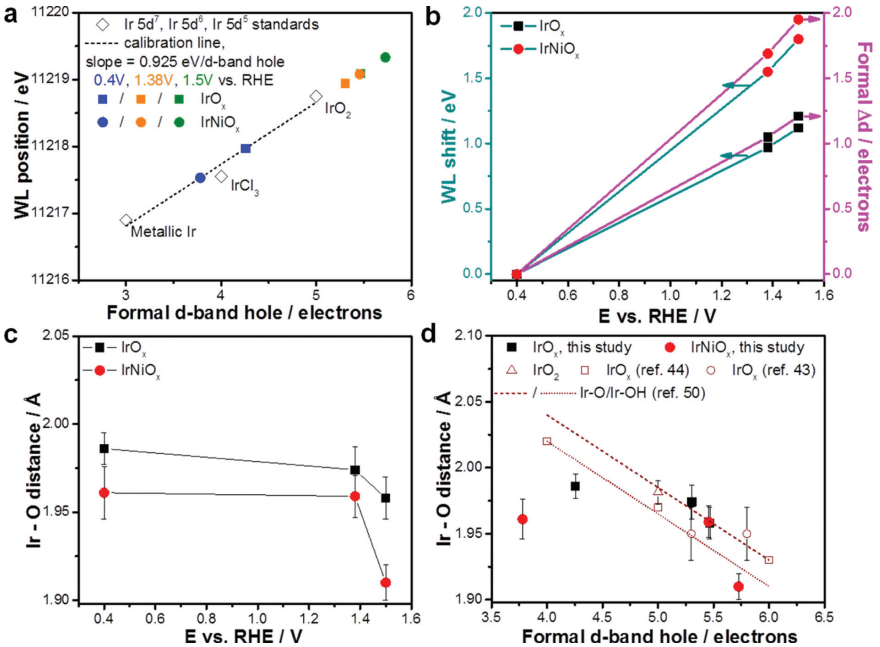

Fig. 5: (a) White line position of IrO_x (squares) and $IrNiO_x$ (circles) as a function of the formal d-band hole count. Formal Δ d values were calculated based on the white line shift and the increase of 0.925 eV per d-band hole calibrated from metallic iridium ($5d^7$), IrCl3 ($5d^6$) and IrO2 ($5d^5$) standards. (b) Energy shift of the white line positions and formal Δ*d* in IrO_x and $IrNiO_x$ nanoparticles at different electrode potentials compared with the corresponding sample at 0.4 VRHE. (c) Ir–O bond distances at different applied potentials. (d) Experimental operando Ir–O bond distances vs. the iridium *d*-band hole count for IrO_x and $IrNiO_x$ nanoparticles from this study (solid black squares and solid red circles, respectively), as well as IrO_x films from previous studies (Ref. [49], empty squares; and Ref. [50], empty circles). The Ir–O distance in the rutile-type IrO_2 standard measured ex-situ in this study is included as reference. The dashed and dotted lines connect the Ir–O and Ir–OH distances, respectively, obtained from the effective ionic radii of Ir^{N+} ions (N = iii, iv or v, corresponding to formal d-band hole counts of four, five or six, respectively) with O^{ii-} or OH^{i-} ions [51]. Error bars in (c) and (d) represent the uncertainties of the bond lengths obtained from the EXAFS simulations. Adapted with permission [45].

IrO_x and $IrNiO_x$ samples. In fact, linear combination fitting of the IrO_x and $IrNiO_x$ XANES regions at +0.4 V_{RHE} confirmed the coexistence of Ir^{iii+} and Ir^{iv+} in both samples at such a low electrode potential, along with a small contribution of the Ir^0 core (12.5%) to the XANES region of IrO_x. For $IrNiO_x$, the larger contribution from the metallic Ir^0 core (61.1%) actually depressed the experimentally observed average number of *d*-band holes below that of IrO_x. When the applied potential was increased from 0.4 to 1.38 V_{RHE}, the white line position of IrO_x and $IrNiO_x$ shifted to higher energy due to the oxidation of iridium sites, as observed in the cyclic voltammogram.

To better understand the OER electrochemistry, we correlated the relative white line shifts with changes in the formal number of iridium *d*-band holes (Δd) in IrO_x and $IrNiO_x$ at the two higher electrode potentials with respect to the number at +0.4 V_{RHE} using the 0.925 eV per *d*-band hole slope. Data in Figure 5b suggests that iridium *d* states in $IrNiO_x$ nanoparticles depopulate more rapidly with electrode potential than those in IrO_x. Given the coexistence of Ir^{iii+} and Ir^{iv+} sites in both IrO_x and $IrNiO_x$ at +0.4 V_{RHE}, the experimentally observed Δd of 1.21 holes for IrO_x at +1.5 V_{RHE} is consistent with the generation of formal Ir^{iv+} and Ir^{v+} sites in IrO_x under OER conditions. On the other hand, the much larger Δd of 1.95 holes for $IrNiO_x$ suggests formal oxidation states approaching Ir^{vi+} in the nickel-leached oxide particle shell under operando oxygen evolution conditions. Even though there is no unanimous consensus on whether redox states above the absolute value of IV+ are sustainable in aqueous solutions, we can unequivocally conclude that nickel-depleted $IrNiO_x$ nanoparticles exhibit significantly increased *d*-band holes (hence, formally higher iridium chemical redox states) during the OER than IrO_x nanoparticles or crystalline rutile-type IrO_2. In other words, the electrochemical removal of nickel atoms from the surface of $IrNiO_x$ nanoparticles and the concomitant electro-oxidation of iridium atoms generates a catalytically highly active type of iridium oxide in the particle shells with a uniquely high number of *d*-band holes. Based on their electronic fingerprint, we will refer to this surface IrO_x phase as hole-doped IrO_x.

To explore the local geometric structure and ligand environment around iridium sites, we performed extended X-ray absorption fine structure (EXAFS) measurements and EXAFS simulations. The simulations of EXAFS spectra revealed the presence of characteristic Ir–O bond distances in the oxidic particle shells and Ir–M (M = Ir or Ni) distances in the metallic cores, confirming the metal oxide hybrid core–shell structures of both IrO_x and $IrNiO_x$. To track the nearest Ir coordination environment of our catalysts under OER conditions, Figure 5c depicts the evolution of Ir–O bond distances in both IrO_x and $IrNiO_x$ with the applied electrode potential. It is common that transition metal–oxygen bond distances decrease with increasing redox state of the central metal ion [52, 57]

because its effective ionic radius decreases. However, when stepping from +0.4 to +1.38 V_{RHE}, the Ir–O distances for each sample stay comparable, although iridium reaches higher redox states. This observation can be explained based on characteristic differences in the iridium ligands, which range from oxo (O), hydroxo (OH) to aqua (OH_2). In anodic IrO_x films prepared by potential cycling metallic iridium films in an acidic environment – similar to the electrochemical protocol applied for the nanoparticles in this study – hydroxo species are dominant at low electrode potential (+0.24 V_{RHE}) [55]. The species undergo deprotonation to oxo species at higher electrode potential (+1.14 and +1.49 V_{RHE}, respectively), while aqua ligands seem to have no strong interaction with the surface [55]. The theoretical Ir–OH distance is shorter than the theoretical Ir–O distance if the iridium oxidation state and coordination number remain the same [51]. In fact, the coordination numbers are comparable at the three electrode potentials; therefore, the deprotonation of hydroxo to oxo ligands offsets redox state effects on bond lengths, thus accounting for the nearly constant Ir–O bond distance in IrO_x and $IrNiO_x$ during iridium oxidation between +0.4 and +1.38 V_{RHE}. The observed Ir–O bond lengths in the IrO_x nanoparticles are in good quantitative agreement with other *in situ* EXAFS studies on IrO_x films and IrO_2 nanoparticles [49, 50, 58]. In contrast, unusually short Ir–O bond lengths in the shells of $IrNiO_x$ nanoparticles, in particular under conditions of oxygen evolution at +1.5 V_{RHE}, were observed.

To emphasize the correlation of the electronic and geometric structures of IrO_x and $IrNiO_x$, Figure 5d shows Ir–O bond distances in IrO_x and $IrNiO_x$ nanoparticles as a function of the formal *d*-band hole count, together with previously reported Ir–O distances in IrO_x films [49, 50]. Theoretical Ir–O and Ir–OH distances (dotted and dashed lines) computed from the effective ionic radii of Ir^{N+} ions with O^{ii-} or OH^{i-} ions are also shown as references [51]. The correlation between datasets in Figure 5d testifies to the very unusual oxygen ligand environment of iridium centres in the shell of $IrNiO_x$ nanoparticles. In particular, our data reveal substantially shorter Ir–O bond lengths (1.91 Å) in nickel-leached electrochemical oxide particle shells compared with conventional iridium oxides [49, 50, 58].

The link between the observed Ir–O bond lengths and change in *d*-band holes can be seen by way of DFT calculations [45]. We computed a series of pristine bulk structures, including rutile-type IrO_2 and the hollandite and romanechite motifs recently observed in amorphous IrO_x samples [59], along with defect structures with varying numbers of iridium/nickel vacancies. Figure 6a shows the computed Δd of the iridium atoms plotted against their change in average computed Ir–O bond length compared with IrO_2. The formally $Ir^{iii}OOH$, which was recently synthesized [60] can be seen to have the longest average Ir–O bond and fewer *d*-band holes than rutile-type IrO_2. All the other crystalline materials, including the hollandite and romanechite types, have a Δd near zero and a computed average Ir–O

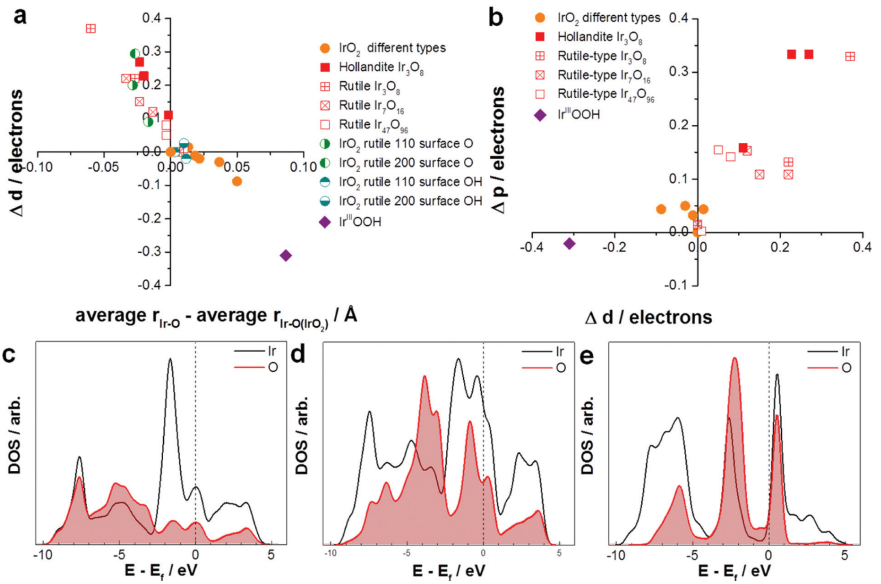

Fig. 6: Computed electronic structure of iridium oxides with various metal-vacancy densities. (a) Computed Δ*d* of the iridium atoms plotted against their change in average computed Ir–O bond length compared with that in rutile-type IrO_2. (b) Computed Δ*p* – the change in the oxygen hole character relative to oxygen in rutile-type IrO_2 – plotted against the computed Δ*d*. (c–e) Projected density of iridium 5*d* and oxygen 2*p* states for rutile-type IrO_2 (c), iridium and oxygen at an iridium vacancy in $Ir_{47}O_{96}$ (d) and iridium and oxygen in the vacancy-rich Ir_3O_8 (e). E, energy; E_f, energy of the Fermi level. Reproduced with permission [45].

bond length near that of rutile-type IrO_2. Introducing defects increases Δ*d* of the iridium atoms near the metal vacancy while simultaneously decreasing the average Ir–O bond length. For the lowest density of metal vacancies, $Ir_{47}O_{96}$, Δ*d* is less than 0.1 electron and the average Ir–O bond remains nearly unchanged compared with that in IrO_2. At higher metal-vacancy densities (that is, Ir_7O_{16}), the average Ir–O bond length of the iridium atoms near the vacancy drops by nearly 0.02 Å, consistent with the IrO_x samples investigated here, although Δ*d* remains below 0.2 electron. It is not until the material becomes extremely defective – with a stoichiometry (Ir_3O_8) – that the average Ir–O bond length drops to values observed for $IrNiO_x$, with a concomitant increase in Δ*d* to ∼0.3–0.4 electron.

The calculations also reveal a profound effect of these short Ir–O bonds on the ligands. To see this, we define (in analogy to Δ*d*) Δ*p* as the change in the oxygen hole character relative to oxygen in rutile-type IrO_2 (Figure 6b), where only the oxygen atoms near the iridium vacancies are considered for the defect structures. At the lowest metal-vacancy density, where $\Delta d < 0.1$ electron, Δ*p* on

the oxygen atoms near the defect can reach 0.2 electron; that is, the oxygen is oxidized, becoming more electrophilic than in rutile-type IrO_2. In the case of the highly defective structures, with an Ir_3O_8 stoichiometry, the short Ir–O bond length leads to increased orbital overlap and a Δp of 0.3 electron. This behaviour can also be seen in the projected density of states (PDOS), where, as the iridium vacancy density increases, the amount of iridium 5*d* and oxygen 2*p* character at ~1 eV above the Fermi energy grows (see Figure 6c–e). In the most extreme case, the average Ir–O bond length reaches those observed for $IrNiO_x$, and the oxygen hole contribution to the ground state becomes so large that the unoccupied states just above the Fermi energy are a near-equal mix of oxygen 2*p* and iridium 5*d* (see Figure 6e).

While bond length contraction could lead to oxygen 2*p* hole formation, inspection of the occupied states suggests that a lowering of the iridium 5*d* states due to an increase in Δd might instead be responsible. The occupied PDOS values show that as the number of iridium vacancies increases, the character of the σ-bonding state at around -7 eV changes from equally mixed oxygen 2*p* and iridium 5*d* to strongly iridium 5*d*. These changes are reminiscent of entering a negative charge-transfer or self-doped regime, where the metal *d* states lie below the oxygen 2*p* before hybridization [61]. Such a situation would result in the appearance of ground-state oxygen holes – which we formally call O^{I-} or, more generally, $O^{(ii\text{-}\delta)-}$. We confirmed that the lowering of the iridium 5*d* states with increasing iridium vacancy concentration is sufficient to produce oxygen holes by computing the PDOS for the vacancy-rich structures without including atomic relaxation. Thus, the increase in Δd drives oxygen hole formation because it pushes the iridium 5*d* states below the oxygen 2*p*.

To see oxygen hole character experimentally, the method of choice is X-ray absorption spectroscopy (XAS) at the O K-edge. We performed such O K-edge XAS measurements with the core-shell $IrNiO_x$ nanoparticles under potential control in 0.05 M H_2SO_4. The precursor alloy $IrNi_{3.3}$ NPs were deposited onto Nafion membranes, which were previously sputtered with ca. 1.4 nm carbon. During NP deposition 8 µL of the NP suspension was added onto the membrane and a potential of +2V were applied to the membrane (as working electrode) for 75 min. Afterwards, membranes were rinsed shortly with absolute ethanol to remove excess NP suspension. Finally, two layers of graphene were deposited onto IrNi NPs/Nafion samples. Graphene was prepared by etching away the Cu side of a Graphene/Cu foil (Graphenea) in 40 g/L ammonium persulfate overnight. The O K-edge spectra were acquired using our homemade cell and a high-pressure XPS/XAS spectrometer. The cell consists of an electrolyte compartment with flowing 0.05 M H_2SO_4, a vacuum chamber, and the Nafion membrane with graphene

on the vacuum side separating these two compartments. *In situ* O K-edge spectra together with a cyclic voltammogram of a representative sample are shown in Figure 7. In the cyclic voltammetry (CV) cycling we see two redox transitions, one at ~1.0–1.1 V, usually assigned to the Ir^{III+}–Ir^{IV+} transition and another one at the onset of OER. The latter is nicely visible in the cathodic scan direction. The OER onset is near 1.5 V. Although the redox transitions and the OER onset are slightly upshifted as compared to those recorded in a standard electrochemical cell, the CV in our *in situ* cell resembles the major features of $IrNiO_x$. The sample was dealloyed and oxidized by CV cycling, and a number of potential points were measured, as indicated in Figure 7b. Clearly, the sample produces electrophilic oxygen (peak at ~529 eV) [62] and shoulder around 528.2 eV under OER conditions (1.674 V). Although the electrocatalyst has some spectral contribution at and above 530 eV, most of the spectral intensity in this higher photon energy range comes from the Nafion membrane and the oxidized graphene. When the potential was decreased below the first iridium redox transition (0.774 V), the 529 eV peak disappeared, but when the potential was reversed back to OER conditions, the signature of electrophilic oxygen re-appeared, suggesting that the true *in situ* state of the sample can by only observed under potential control and in contact with the electrolyte. Thus, experiments and theory are in agreement that iridium oxidation drives the formation of holes on oxygen ligands under OER conditions and Ni leaching during catalyst activation generates lattice vacancies that produce highly active oxygen configurations with enhanced reactivity.

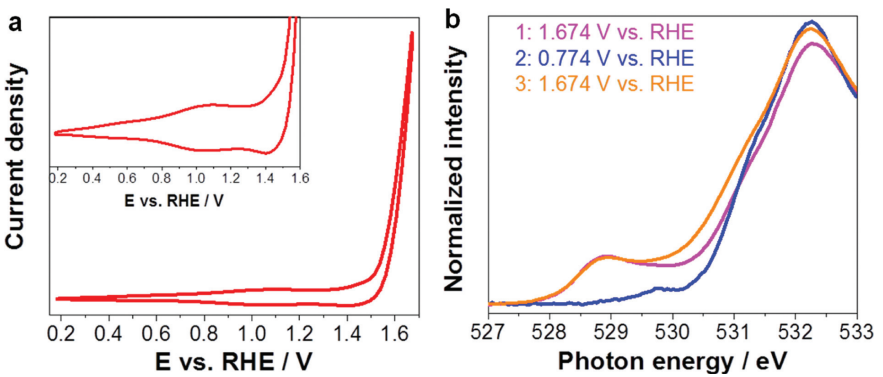

Fig. 7: (a) Cyclic voltammetry (CV) of IrNi nanoparticles measured in the *in situ* XPS-XAS cell with a scan rate of 100 mV s^{-1}. Inset shows the redox features and the OER onset range. (b) O K-edge spectra of IrNi nanoparticles at different electrode potentials measured in the order of 1: 1.674 V, 2: 0.774 V, and 3: 1.674 V vs. RHE. Electrolyte: 0.05 M H_2SO_4.

2.3 Photovoltaic-biased electrosynthetic cell (PV-EC) test with $IrNiO_x$

$IrNiO_x$ was utilized as OER catalyst in a photovoltaic-biased electrosynthetic cell (PV-EC device) based on a triple junction solar cell (Figure 8a). The integrated PV-EC device consists of four main components: (1) The triple junction solar cell (a–Si–H/a–Si:H/μc–Si:H) with an open circuit voltage (V_{OC}) of 2.2 V, current density at the maximum power point (J_{MPP}) of 6.0 mA cm^{-2}, photovoltaic efficiency of 10.7%, fill factor (FF) of 72%, and short circuit current density (J_{SC}) of 6.8 mA cm^{-2}. (2) A catalyst layer to improve HER consisting of electrodeposited Pt nanoparticles. (3) The electrolyte; and (4) an $IrNiO_x$ coated Ti plate as the anode.

The photoelectrochemical performance of the PV-EC device was measured in 1 M and 0.1 M H_2SO_4 solution under simulated AM 1.5 solar illumination (100 mW cm^{-2}) using a two-electrode setup. The cyclic voltammetry curves (CVs) (Figure 8b) show that it works slightly above the MPP of the PV-EC device, indicating that the tested electrocatalysts are not the limiting factors in the performance of this PV-EC arrangement. The chronoamperometry stability tests (Figure 8c) at

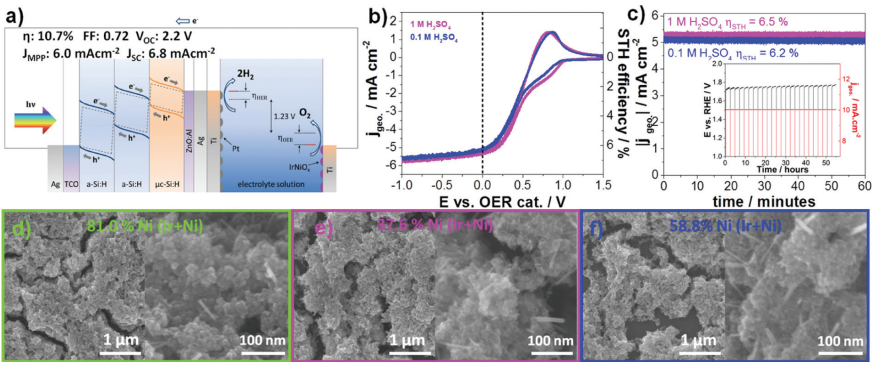

Fig. 8: (a) Band diagram illustration of the PV-EC device configuration and PV parameters of the used triple junction solar cell. (b) Cyclic voltammetry (CVs) measured with 50 mV s^{-1} and the corresponding solar-to-hydrogen (STH) efficiencies. PV-EC tests were carried out in 1 M and 0.1 M H_2SO_4 using a 2-electrode setup with triple junction cell (see (a)), electrodeposited Pt HER-catalyst and activated $Ir(Ni)O_x$ OER-catalyst (Activation: 50 cycles, 500 mV s^{-1}, 1 M H_2SO_4, 0.05–1.5 V vs. RHE) under AM 1.5 illumination (100 mW cm^{-2}). (c) Chronoamperometric stability measurements at 0 V applied bias for the 2-electrode PV-EC setup. Inset is the galvanostatic stability test at a current density of 10 mA cm^{-2} performed in 0.05 M H_2SO_4 using a 3-electrode setup with Pt mesh as counter electrode and $IrNiO_x$ as the working electrode (OER anode) without illumination. (d, e, f) SEM images and Ni contents (measured by EDX) of $IrNiO_x$ catalysts at as-prepared state (d), after PV-EC test in 1 M H_2SO_4 (e), and after PV-EC test in 0.1 M H_2SO_4 (f).

0 V applied bias show stable photocurrents over the course of 1 h for both electrolytes, the current densities correspond to solar-to-hydrogen (STH) efficiencies of 6.5% and 6.2% (assuming 100% faradaic efficiency) for the measurements in 1 M and 0.1 M H_2SO_4, respectively. Galvanostatic test of the $IrNiO_x$ catalyst at a current density of 10 mA cm^{-2} using a 3-electrode setup without illumination (Figure c inset) highlights the stability of the OER catalyst. The electrode potential was stable under the course of over 50 h.

SEM images of the as-prepared $IrNiO_x$ anode (Figure 8d) show the porous morphology of the catalyst layer with a mud-crack structure. At high magnification, besides the primarily interconnected spherical particles, some fine needle-shaped structures are observed, which can presumably be attributed to segregated iridium oxide [33]. After PV-EC tests in 1 M and 0.1 M H_2SO_4, the grains became less defined and more porous. EDX indicates the morphology changes are linked to Ni leaching, the Ni content (vs. total Ir and Ni) decreased from 81.0% in the as-prepared sample to 37.6% and 58.8% in 1 M and 0.1 M H_2SO_4-tested samples, respectively.

3 Conclusions and outlook

In this mini review, we have highlighted selected advances in our understanding of Ir–Ni bimetallic oxide electrocatalysts for the OER in acidic environments.

Ir–Ni bimetallic oxide thin films offer significantly improved geometric, mass-based, and real surface based electrocatalytic OER reactivities, even if the catalyst synthesis is conducted at elevated annealing temperatures, such as 450 °C, where pure Ir oxide catalyst yield consistently lower OER reactivities. The elevated annealing temperature are beneficial for the mechanical and electrochemical stability of the bimetallic oxide films. Data showed that the Ni doping of Ir oxides delay the crystallization of the bimetallic Ir–Ni oxide films. Upon exposure to acidic electrolytes, the electrochemical dissolution of Ni ion into the electrolyte leaves behind an amorphous hydrous IrO_x surface characterized by a very high degree of surface hydroxylation, which, for pure Ir oxide films, can only be obtained at much lower film annealing temperatures that are associated with stronger corrosive instabilities of these films of around 2.5 ng_{Ir} mC^{-1}. In other words, Ni atoms aided in achieving preferable chemical surface terminations under preparation conditions that are beneficial from a stability point of view.

Further experimental studies explored the chemical nature and chemical state of the reactive surface hydroxyls in Ni-depleted Ir oxide films and dealloyed $IrNi@IrO_x$ nanoparticles. The generation of Ir lattice vacancies in the activated OER catalysts, caused by acidic Ni leaching, increased the d holes character of Ir

and resulted in much shortened local Ir–O bond distances. In addition, Ni leaching from Ir–Ni mixed oxides also resulted in the concurrent generation of O p holes in the activated catalysts. DFT-based computational results indicated that Ni doping into rutile IrO_2 lattices, replacing Ir with Ni, followed by Ni dissolution from the lattice results in a lattice-vacancy-rich, electron hole-doped lattice, where positive holes are located on both the metal ion centers and on the oxygen ligands in agreement with the spectroscopic measurements. Increases in Ir d hole character is closely correlated with increases in O p hole character. As a result of this, the electrophilic oxygen ligands, owing to their hole character, offer reduced kinetic barriers to the nucleophilic attack by water molecules. In that process bridging or terminal O ligands in sufficient proximity act as hydrogen acceptors. It is our conviction that most, if not all, other previously described Ir-based multimetallic catalyst concepts and systems, for instance multi-metal Iridate perovskite materials, follow closely the outlined activation mechanism in acidic solutions involving initial surface metal leaching. After the metal leaching has reached completion or a low reaction rate, a core-shell type structure is established. The highly lattice defective, hydroxylated Ir oxide displays favorable OER reaction rates due to the (re)generation of catalytically active electrophilic oxygen ligands in their highly defective Ir oxide lattices.

More generally, the presented data suggests that electrochemically leached, hydroxyl-rich Ir oxide of any kind should follow the geometric and electronic structure transformation outlined above. Their enhanced hole-doped state with electrophilic oxygen ligands is highly conducive to improved catalytic water oxidation rates, at least up to the range of 10 mA cm^{-2} tested. Whether or not sacrificial dopants such as Ni discussed here provides a beneficial effect on the OER rates at industrially relevant current densities, this still needs to be confirmed. The activated Ni-depleted Ir oxide OER catalyst were finally deployed as anode catalysts on the oxidic passivation layer of multi-junction photoelectrochemical cells and exhibited good solar to hydrogen efficiencies and sustained STH efficiencies over 1 h of continued operation.

In a somewhat broader context, the comparison of the catalytic performance of leached $IrNiO_x$ core-shell nanocatalysts [33, 45] to other Ir-based nanoparticle catalyst concepts [41, 63–65] as well as non-precious metal-based electrocatalyst concepts, such as electrodeposited hydrous Cobalt oxides or Nickel oxides [66, 67], reveals a significant efficiency benefit of the present Ni-leached $IrNiO_x$-based nanoparticles in terms of kinetic overpotential of the OER as well as stability benefit due to the corrosive nature of the noble metal-free concepts in acidic electrolyzes. In alkaline conditions, the present $IrNiO_x$ catalysts as well as previously reported Ir-based catalysts [68] perform comparable to their noble

metal free counterparts in terms of efficiency and stability. However, a direct comparison of catalysts that unfold their optimum performance under vastly different operating conditions, such as Ni–Fe-oxides in strongly alkaline or Iridium-based catalysts in strongly acidic conditions, is notoriously problematic and of little practical merit. In addition, it should be noted that the catalyst cost, be it precious or non-precious, at today's production scales are rather insignificant compared to input electricity cost (PV-Electrolyzer schemes) or cost of other PEC cell components. Acidic conditions are considered the preferred mode of operation of Polymer Electrolyte Membrane Water Electrolyzers (PEMWEs) where cell efficiency is the primary focus, because input electricity is controlling the overall total cost of ownership. This is because alkaline operating conditions generally cause additional efficiency losses at the HER catalysts as well as the OER catalysts, and, on top, additional ohmic losses arise due to lower hydroxyl ion mobility. On the other hand, alkaline conditions are preferred where efficiency considerations are secondary and focus is entirely placed on catalyst or device cost. This may be the case for small-scale PEC systems. The lower alkaline efficiency, however, will eventually require larger active cell areas at a given required hydrogen yield, which typically drives up the total cost of larger-scale PEC systems due to the need of larger quantities of the non-catalyst cell components (membrane, semiconductor, electrolyte, etc.). Hence, for both PEMWEs and PECs, catalyst and cell efficiency often trumps catalyst cost.

Concerning future deployment of leached bimetallic Ir oxides on the anode of photoelectrochemical cells, more work needs to be done to understand the interaction of oxidic catalysts with their supporting backing layers. This is because catalyst studies to date often do not include the effect of supports and backings pertinent to PECs. Here future work must focus on the typical backing layer materials used in both buried junction PEC schemes, as well as selected oxidic materials of non-buried junction PECs [69].

Acknowledgements: Financial support by the German Research Foundation (DFG) under the Priority Program 1613 is gratefully acknowledged. We thank the HZB for allocation of synchrotron radiation beamtime.

References

1. J. L. Sawin, F. Sverrisson, J. Rutovitz, S. Dwyer, S. Teske, H. E. Murdock, R. Adib, F. Guerra, H. E. Murdock, L. H. Blanning, F. Guerra, V. Hamirwasia, A. Misra, K. Satzinger, L. E. Williamson, M. Lie, A. Nilsson, E. Aberg, S. Weckend, H. Wuester, R. Ferroukhi, C. Garcia, A. Khalid, M. Renner, M. Taylor, B. Epp, K. Seyboth, J. Skeen, G. Kamiya, L. Munuera, F. Appavou, A. Brown, B. Kondev, E. Musolino, A. Brown, L. Mastny, L. Arris,

Renewables 2018 – Global status report A comprehensive annual overview of the state of renewable energy Advancing the global renewable energy transition – Highlights of the REN21 Renewables 2018 Global Status Report in perspective; 978-3-9818911-3-3; France (2018), P. 542.
2. N. S. Lewis, D. G. Nocera, Proc. Natl. Acad. Sci. U.S.A. **103** (2006) 15729.
3. T. da Silva Veras, T. S. Mozer, D. da Costa Rubim Messeder dos Santos, A. da Silva César, Int. J. Hydrogen Energy **42** (2017) 2018.
4. F. M. Sapountzi, J. M. Gracia, C. J. Weststrate, H. O. A. Fredriksson, J. W. Niemantsverdriet, Progr. Energy Combust. Sci. **58** (2017) 1.
5. F. F. Abdi, L. Han, A. H. M. Smets, M. Zeman, B. Dam, R. van de Krol, Nat. Commun. **4** (2013) 2195.
6. J. W. Ager, M. R. Shaner, K. A. Walczak, I. D. Sharp, S. Ardo, Energy Environ. Sci. **8** (2015) 2811.
7. M. M. May, H.-J. Lewerenz, D. Lackner, F. Dimroth, T. Hannappel, Nat. Commun. **6** (2015) 8286.
8. D. G. Nocera, Acc. Chem. Res. **45** (2012) 767.
9. F. Urbain, V. Smirnov, J.-P. Becker, A. Lambertz, F. Yang, J. Ziegler, B. Kaiser, W. Jaegermann, U. Rau, F. Finger, Energy Environ. Sci. **9** (2016) 145.
10. M. Carmo, D. L. Fritz, J. Merge, D. Stolten, Int. J. Hydrogen Energy **38** (2013) 4901.
11. J. Mergel, M. Carmo, D. Fritz, In: Transition to Renewable Energy Systems, D. Stolten, V. Scherer, Eds. Wiley-VCH Verlag GmbH & Co. KGaA, Weinheim, Germany (2013), P. 423–450.
12. F. Dionigi, T. Reier, Z. Pawolek, M. Gliech, P. Strasser, ChemSusChem. **9** (2016) 962.
13. F. Dionigi, P. Strasser, Adv. Energy Mater. **6** (2016) 1600621.
14. T. Reier, M. Oezaslan, P. Strasser, ACS Catal. **2** (2012) 1765.
15. D. Todd, M. Schwager, W. Mérida, J. Power Sources **269** (2014) 424.
16. C. Spöri, J. T. H. Kwan, A. Bonakdarpour, D. P. Wilkinson, P. Strasser, Angew. Chem. Int. Ed. **56** (2017) 5994.
17. F. E. Osterloh, Chem. Soc. Rev. **42** (2013) 2294.
18. J. O. Bockris, J. Chem. Phys. **24** (1956) 817.
19. S. Trasatti, J. Electroanal. Chem. **111** (1980) 125.
20. W. T. Hong, M. Risch, K. A. Stoerzinger, A. Grimaud, J. Suntivich, Y. Shao-Horn, Energy Environ. Sci. **8** (2015) 1404.
21. J. Rossmeisl, A. Logadottir, J. K. Nørskov, Chem. Phys. **319** (2005) 178.
22. H. Dau, C. Limberg, T. Reier, M. Risch, S. Roggan, P. Strasser, ChemCatChem. **2** (2010) 724.
23. I. C. Man, H.-Y. Su, F. Calle-Vallejo, H. A. Hansen, J. I. Martínez, N. G. Inoglu, J. Kitchin, T. F. Jaramillo, J. K. Nørskov, J. Rossmeisl, ChemCatChem. **3** (2011) 1159.
24. J. Rossmeisl, Z. W. Qu, H. Zhu, G. J. Kroes, J. K. Nørskov, J. Electroanal. Chem. **607** (2007) 83.
25. T. Reier, H. N. Nong, D. Teschner, R. Schlögl, P. Strasser, Adv. Energy Mater. **7** (2017) 1601275.
26. S. Cherevko, S. Geiger, O. Kasian, N. Kulyk, J.-P. Grote, A. Savan, B. R. Shrestha, S. Merzlikin, B. Breitbach, A. Ludwig, K. J. J. Mayrhofer, Catal. Today **262**(Supplement C) (2016) 170.
27. S. Cherevko, T. Reier, A. R. Zeradjanin, Z. Pawolek, P. Strasser, K. J. J. Mayrhofer, Electrochem. Commun. **48**(Supplement C) (2014) 81.
28. L. Gan, M. Heggen, R. O'Malley, B. Theobald, P. Strasser, Nano Lett. **13** (2013) 1131.

29. C. Cui, L. Gan, H. H. Li, S. H. Yu, M. Heggen, P. Strasser, Nano Lett. **12** (2012) 5885.
30. B. Han, C. E. Carlton, A. Kongkanand, R. S. Kukreja, B. R. Theobald, L. Gan, R. O'Malley, P. Strasser, F. T. Wagner, Y. Shao-Horn, Energy Environ. Sci. **8** (2015) 258.
31. C. Baldizzone, L. Gan, N. Hodnik, G. P. Keeley, A. Kostka, M. Heggen, P. Strasser, K. J. J. Mayrhofer, ACS Catal. **5** (2015) 5000.
32. S. Rudi, L. Gan, C. Cui, M. Gliech, P. Strasser, J. Electrochem. Soc. **162** (2015) F403.
33. T. Reier, Z. Pawolek, S. Cherevko, M. Bruns, T. Jones, D. Teschner, S. Selve, A. Bergmann, H. N. Nong, R. Schlögl, K. J. J. Mayrhofer, P. Strasser, J. Am. Chem. Soc. **137** (2015) 13031.
34. S. Cherevko, A. Topalov, A. Zeradjanin, G. Keeley, K. J. Mayrhofer, Electrocatalysis **5** (2014) 235.
35. S. Cherevko, A. R. Zeradjanin, A. A. Topalov, N. Kulyk, I. Katsounaros, K. J. J. Mayrhofer, ChemCatChem. **6** (2014) 2219.
36. S. Geiger, O. Kasian, M. Ledendecker, E. Pizzutilo, A. M. Mingers, W. T. Fu, O. Diaz-Morales, Z. Li, T. Oellers, L. Fruchter, A. Ludwig, K. J. J. Mayrhofer, M. T. M. Koper, S. Cherevko, Nat. Catal. **1** (2018) 508.
37. A. P. Grosvenor, B. A. Kobe, N. S. McIntyre, Surf. Sci. **572** (2004) 217.
38. T. Reier, D. Teschner, T. Lunkenbein, A. Bergmann, S. Selve, R. Kraehnert, R. Schlögl, P. Strasser, J. Electrochem. Soc. **161** (2014) F876.
39. K. Ahrenstorf, O. Albrecht, H. Heller, A. Kornowski, D. Görlitz, H. Weller, Small **3** (2007) 271.
40. H. N. Nong, L. Gan, E. Willinger, D. Teschner, P. Strasser, Chem. Sci. **5** (2014) 2955.
41. Y. Lee, J. Suntivich, K. J. May, E. E. Perry, Y. Shao-Horn, J. Phys. Chem. Lett. **3** (2012) 399.
42. H.-S. Oh, H. N. Nong, P. Strasser, Adv. Funct. Mater. **25** (2015) 1074.
43. H. N. Nong, H. S. Oh, T. Reier, E. Willinger, M. G. Willinger, V. Petkov, D. Teschner, P. Strasser, Angew. Chem. Int. Ed. **54** (2015) 2975.
44. S. Geiger, O. Kasian, A. M. Mingers, S. S. Nicley, K. Haenen, K. J. J. Mayrhofer, S. Cherevko, ChemSusChem. **10** (2017) 4140.
45. H. N. Nong, T. Reier, H.-S. Oh, M. Gliech, P. Paciok, T. H. T. Vu, D. Teschner, M. Heggen, V. Petkov, R. Schlögl, T. Jones, P. Strasser, Nat. Catal. **1** (2018) 841.
46. M. Brown, R. E. Peierls, E. A. Stern, Phys. Rev. B **15** (1977) 738.
47. J. H. Choy, D. K. Kim, G. Demazeau, D. Y. Jung, J. Phys. Chem. **98** (1994) 6258.
48. J. P. Clancy, N. Chen, C. Y. Kim, W. F. Chen, K. W. Plumb, B. C. Jeon, T. W. Noh, Y.-J. Kim, Phys. Rev. B **86** (2012) 195131.
49. Y. Mo, I. C. Stefan, W.-B. Cai, J. Dong, P. Carey, D. A. Scherson, J. Phys. Chem. B **106** (2002) 3681.
50. A. R. Hillman, M. A. Skopek, S. J. Gurman, Phys. Chem. Chem. Phys. **13** (2011) 5252.
51. R. Shannon, Acta Cryst. **32** (1976) 751.
52. J.-H. Choy, D.-K. Kim, S.-H. Hwang, G. Demazeau, D.-Y. Jung, J. Am. Chem. Soc. **117** (1995) 8557.
53. B. E. Conway, J. Mozota, Electrochim. Acta **28** (1983) 9.
54. E. J. Frazer, R. Woods, J. Electroanal. Chem. **102** (1979) 127.
55. R. Kötz, H. Neff, S. Stucki, J. Electrochem. Soc. **131** (1984) 72.
56. J. Mozota, B. E. Conway, Electrochim. Acta **28** (1983) 1.
57. M. Görlin, P. Chernev, J. Ferreira de Araújo, T. Reier, S. Dresp, B. Paul, R. Krähnert, H. Dau, P. Strasser, J. Am. Chem. Soc. **138** (2016) 5603.
58. D. F. Abbott, D. Lebedev, K. Waltar, M. Povia, M. Nachtegaal, E. Fabbri, C. Copéret, T. J. Schmidt, Chem. Mater. **28** (2016) 6591.

59. E. Willinger, C. Massué, R. Schlögl, M. G. Willinger, J. Am. Chem. Soc. **138** (2017) 12093.
60. D. Weber, L. M. Schoop, D. Wurmbrand, J. Nuss, E. M. Seibel, F. F. Tafti, H. Ji, R. J. Cava, R. E. Dinnebier, B. V. Lotsch, Chem. Mater. **29** (2017) 8338.
61. A. V. Ushakov, S. V. Streltsov, D. I. Khomskii, J. Phys. Condens. Matter. **23** (2011) 445601.
62. V. Pfeifer, T. E. Jones, J. J. Velasco Velez, R. Arrigo, S. Piccinin, M. Havecker, A. Knop-Gericke, R. Schlogl, Chem. Sci. **8** (2017) 2143.
63. C. Wang, Y. Sui, G. Xiao, X. Yang, Y. Wei, G. Zou, B. Zou, J. Mater. Chem. A **3** (2015) 19669.
64. P. Lettenmeier, L. Wang, U. Golla-Schindler, P. Gazdzicki, N. A. Cañas, M. Handl, R. Hiesgen, S. S. Hosseiny, A. S. Gago, K. A. Friedrich, Angew. Chem. Int. Ed. **55** (2016) 742.
65. A. Grimaud, A. Demortière, M. Saubanère, W. Dachraoui, M. Duchamp, M.-L. Doublet, J.-M. Tarascon, Nat. Energy **2** (2016) 16189.
66. M. W. Kanan, D. G. Nocera, Science **321** (2008) 1072.
67. T. W. Kim, K.-S. Choi, Science **343** (2014) 990.
68. L. C. Seitz, C. F. Dickens, K. Nishio, Y. Hikita, J. Montoya, A. Doyle, C. Kirk, A. Vojvodic, H. Y. Hwang, J. K. Norskov, T. F. Jaramillo, Science **353** (2016) 1011.
69. V. Andrei, R. L. Z. Hoye, M. Crespo-Quesada, M. Bajada, S. Ahmad, M. De Volder, R. Friend, E. Reisner, Adv. Energy Mater. **8** (2018) 1801403.